Flame Bands: CO + O chemiluminescence as a measure of gas temperature

G. Raposo[1], A.W. van de Steeg[2], E.R. Mercer[3], C.F.A.M. van Deursen[2], H.J.L. Hendrickx[2], W.A. Bongers[2], G.J. van Rooij[2,4], M.C.M. van de Sanden[2,5] and F.J.J. Peeters[2*]

[1] Instituto Superior Técnico, Lisbon, Portugal
[2] DIFFER, Eindhoven, the Netherlands
[3] University of Antwerp, Antwerp, Belgium
[4] Maastricht University, Maastricht, The Netherlands
[5] Eindhoven University of Technology, Eindhoven, The Netherlands

**Corresponding author: f.j.j.peeters@differ.nl*

Abstract

Carbon monoxide flame band emission ($CO + O \rightarrow CO_2 + h\nu$) in CO_2 microwave plasma is quantified by obtaining absolute emission spectra at various locations in the plasma afterglow while simultaneously measuring gas temperatures using rotational Raman scattering. Comparison of our results to literature reveals a contribution of O_2 Schumann-Runge UV emission at $T > 1500$ K. This UV component likely results from the collisional exchange of energy between $CO_2(^1B)$ and O_2. Limiting further analysis to $T < 1500$ K, we demonstrate the utility of CO flame band emission by analyzing afterglows at different plasma conditions. We show that the highest energy efficiency for CO production coincides with an operating condition where very little heat has been lost to the environment prior to ~ 3 cm downstream, while simultaneously, T ends up below the level required to effectively freeze in CO. This observation demonstrates that, in CO_2 plasma conversion, optimizing for energy efficiency does not require a sophisticated downstream cooling method.

1. Introduction

Carbon monoxide flame bands are the result of recombination of CO and O to a highly excited electronic state of CO_2 and consist of broadband emission of visible radiation, with extension into the UV. With ground state $CO(^1\sum_g^+)$ and ground state $O(^3P)$ having different spin quantum numbers, a direct recombination to ground state $CO_2(^1\widetilde{X}\sum_g^+)$ cannot occur [1,2]. The recombination process must instead result from a chain of reactions such as:

$$CO(^1\sum_g^+) + O(^3P) + M \leftrightarrow CO_2(1\,^3B_2\,\sum_u^+) + M, \quad (R1)$$

$$CO_2(1\,^3B_2\,\sum_u^+) + M \leftrightarrow CO_2(1\,^1B_2\,\Delta_u) + M, \quad (R2)$$

$$CO_2(1\,^1B_2\,\Delta_u) + M \rightarrow CO_2(^1\widetilde{X}\sum_g^+) + M \text{ and} \quad (R3)$$

$$CO_2(1\,^1B_2\,\Delta_u) \rightarrow CO_2(^1\widetilde{X}\sum_g^+) + h\nu, \quad (R4)$$

where the initial recombination R1 leads to excited CO_2 in a triplet state, which can undergo a (collision-induced) crossing over to excited CO_2 in a singlet state via R2, which in turn can either be quenched to the ground state or undergo a radiative transition to the ground state of CO_2 via R3 or R4, respectively [2–4]. It is the latter reaction which produces CO flame band emission. From this point onwards, the triplet state will be referred to as $CO_2(^3B)$, the singlet as $CO_2(^1B)$ and the ground states of all species simply as CO, O and CO_2. It is important to note here that first principles calculations have revealed a significant overlap in the lowest electronically excited states of CO_2, so that $CO_2(^3B)$ and $CO_2(^1B)$ could be substituted by $CO_2(^3A)$ and $CO_2(^1A)$ [5,6]. The general scheme of R1 - R4 is assumed to be applicable

in either case since energy levels and dissociation limits for both singlets and triplets are *approximately* equal [2]. A schematic potential energy diagram along the OC-O bond length for CO_2, $CO_2(^3B)$ and $CO_2(^1B)$ is depicted in Figure 1, which also includes the relative potential energy curve for the $O_2(^3B)$ state. The $O_2(^3B)$ state leads to O_2 Schumann-Runge emission between 180 – 450 nm and has been observed in conjunction with CO flame band emission in CO_2 mixtures [4].

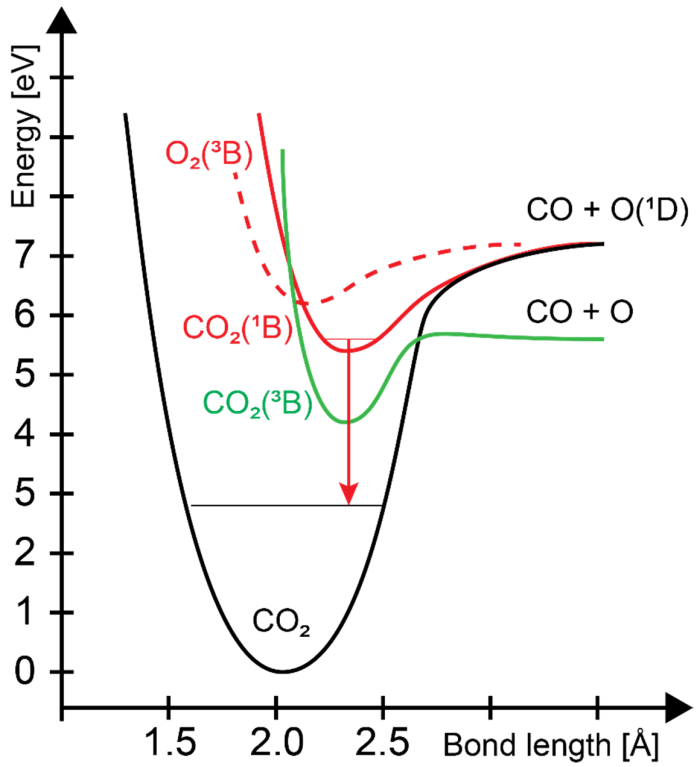

Figure 1: *Schematic potential energy diagram along the OC-O bond length for CO_2, $CO_2(^3B)$ and $CO_2(^1B)$. The dashed line indicates the potential energy in $O_2(^3B)$ leading to O_2 Schumann-Runge emission bands between 180 – 450 nm, which is included here for comparison without the O-O bond length being to scale* [7]. *CO_2 and $CO_2(^1B)$ dissociate into CO + $O(^1D)$ while $CO_2(^3B)$ dissociates into CO and O. The crossing over between $CO_2(^3B)$ and $CO_2(^1B)$ via R2 occurs where the green solid line and the red solid line overlap. The red arrow indicates a radiative transition from $CO_2(^1B)$ to CO_2.*

Carbon monoxide flame band emission in a CO/O_2 flame was first studied spectrographically by Burch in 1885 and 1886 [8,9], who reported a broadband emission spectrum across the visible range with different maxima in the green and violet. A more detailed investigation was performed by Weston in 1925 in CO/O_2 and $CO/H_2/O_2$ flames [10,11], from which it was concluded that the spectrum consists of a continuous background, with distinct, superimposed emission bands. Gaydon [12] and Clyne & Thrush [12,13] were the first to confirm the origins of CO flame bands via the recombination reaction R1. Dixon assigned its component bands to transitions between $CO_2(^1B, \nu_1 = \nu_2 = \nu_3 = 0, 1) \rightarrow CO_2(2\nu_1+\nu_2 = 20 – 30, \nu_3 = 0,1)$ for wavelengths between 310 nm – 380 nm [14]. Because the upper electronic state $CO_2(^1B)$ is a strongly bent molecule, transitions to the linear ground state predominantly populate $2\nu_1+\nu_2$, instead of the asymmetric stretching mode ν_3. The reactions R1 – R4, then, predominantly produce ground state CO_2 with highly excited combinations of the symmetric stretching mode ν_1 and bending mode ν_2[15]. Since each of the many possible transitions brings with it a P- and R-branch, the resulting rovibrational spectrum is very dense in overlapping spectral features, creating a quasi-

continuous spectrum if observed with spectral resolutions less than 0.005 nm, explaining the continuum features observed by Burch and Weston. The aforementioned experiments in CO-containing flames at temperatures ≤ 2200 K were eventually supplemented by experiments in shock tubes, with which the temperature range for observing CO flame band emission was extended towards 3000 K [4,16,17].

The goal of this work is to map CO flame band spectra not in CO-containing flames, but in CO_2 plasma afterglows at various temperatures, with the purpose of using the spectral shape of the quasi-continuum as a measure of gas temperature. The absolute photon emission together with gas temperature can also serve as a measure for the CO + O recombination rate, or be used to obtain quantitative data on CO and O densities. Measuring absolute CO flame band emission at two or three specific wavelengths can allow for a fast 2D mapping of both gas temperature and the rate of back reactions occurring in the near-plasma and downstream portions of CO_2 plasma devices. This can be a valuable diagnostic for evaluating reactor performance or plasma model validation.

Two similar vortex-stabilized CO_2 microwave plasma reactors are used in this work. One is equipped for laser Raman scattering to obtain gas temperatures independently [18,19], and another is equipped for measuring CO flame band spectra over a large part of the afterglow using stepper motors. These reactors possess very high local plasma power densities of > 1 GW/m^3 and large radial temperature gradients on the order of 2500 K/cm [20,21]. Due to the high plasma gas temperatures of > 3500 K almost complete dissociation of CO_2 to CO + O occurs within the plasma region [19,21], which results in a luminous afterglow in the region surrounding the plasma. See Figure 2 for a photograph of the second plasma reactor used for large-scale afterglow mapping. With a high local CO and O density and a broad range of gas temperatures, these plasma reactors are well suited for studying CO flame band emission as a diagnostic tool in a pure CO_2 plasma environment .

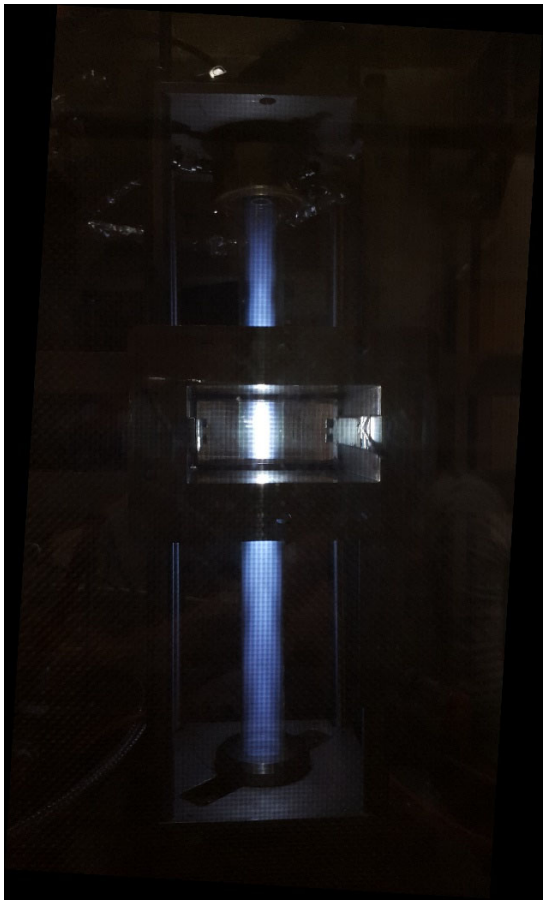

Figure 2: *Photograph of the vortex-stabilized microwave plasma reactor used for complete mapping of afterglows (operated here with a CO_2 flow of 10 slm, pressure of 100 mbar and a microwave power of 1 kW). The plasma in the center of the waveguide is white, while blue afterglows extend above and below the waveguide, within the vortex flow structure created by tangential injection of CO_2 at the top.*

2. Theory & Approach

It has been empirically observed that reaction chains such as R1 - R4 can be expressed as a second order reaction [4,22,23], producing a wavelength-integrated emission intensity

$$I_\gamma = k_\gamma(T)[\mathrm{CO}][\mathrm{O}], \tag{1}$$

in units of photons.m^{-3}s^{-1}, with [CO] and [O] the carbon monoxide and atomic oxygen number densities in m^{-3} and k_γ the rate coefficient in units of photons.m^{3}s^{-1}. Throughout this work $k_\gamma(T) = 1.14 \cdot 10^{-24} e^{-\frac{2080}{T}}$ photons.m^{-3}s^{-1} is assumed, based on measurements obtained by Slack & Grillo [23] and Myers & Bartle [4] for a temperature range of 1300 – 3000 K in a wavelength range of 260 – 800 nm. Note also that all results will be presented assuming a 4π solid angle, so that steradians are not included in the units.

The details of how the rate coefficient k_γ relates to proposed reaction chains such as R1 - R4 has been an object of study for many decades, motivated by *e.g.* the use of the emission intensity I_γ as a means to determine the overall rate coefficient k_{rec} for the CO + O recombination reaction [24,25]:

$$CO + O + M \rightarrow CO_2 + M. \quad \text{(R5)}$$

A complete analysis of the various competing reaction chains in the literature is beyond the scope of this work, but an analysis for the reactions R1 - R4 is presented in the Supplementary Information. Here it suffices to mention a few general features:

- For most combinations of pressure and temperature, the quenching rate via R3 outstrips the spontaneous emission rate via R4, producing a simple relation between the (3rd order) overall recombination rate coefficient and the (2nd order) photon emission rate coefficient:

$$\frac{k_{rec}}{k_\gamma} = \frac{k_3^+}{k_4^+}, \quad (2)$$

  in units of m^3. With the spontaneous emission rate k_4^+ independent of temperature, and the quenching rate coefficient k_3^+ typically assumed only weakly dependent on temperature, Eq. (2) illustrates the direct correspondence between k_γ and k_{rec}. The value of this ratio is typically on the order of 10^{20} m^{-3} at T > 1000 K [4,23,26,27].
- The identity of the third particle in the reaction chain has a limited effect on the value of k_γ, with M = Ar, He, N_2, O_2 being the most thoroughly tested [28–30]. Pravilov and Smirnova have shown that O_2 can reduce k_γ by 10% for $[O_2] > 2\cdot10^{21}$ m^{-3} for total pressures < 20 mbar and T < 300 K [3]. Third particle efficiencies for the overall reaction R5 with rate coefficient k_{rec} are summarized in a review by Baulch *et al.* [31], revealing an order of efficiencies He/Ne < Ar < N_2 < CO < CO_2 < O_2 with at least an order of magnitude difference from lowest to highest. Since k_{rec} scales directly with k_3^+, the third particle identity can significantly affect the ratio in Eq. (2) but may still leave the rate coefficient k_γ largely unaffected (see the Supplementary Information).
- The reaction chain R1 – R4 involves multiple collisions with a third particle M before $CO_2(^1B)$ is formed, and the expected natural radiative lifetime of the $CO_2(^1B)$ state is on the order of 100 ns [3,29]. It can be assumed that $CO_2(^1B)$ is fully thermalized prior to the emission of a photon, since at the conditions investigated here, neutral-neutral collision frequency is estimated to be at least 50 times greater than the radiative lifetime of $CO_2(^1B)$.

The main objective of this work is not to utilize wavelength-integrated photon emission intensities, but to infer gas temperatures from measured CO flame band spectra. Here we run into shortcomings of the current literature: transition moments for $CO_2(^1B, \nu_1, \nu_2, \nu_3 > 0) \rightarrow CO_2(2\nu_1+\nu_2 > 20, \nu_3 > 0)$ are unavailable. Many first principles computational studies have focused on the inverse problem of CO_2 photolysis, where ground state CO_2 in low vibrational states is excited by UV photons to the $CO_2(^1A)$ or $CO_2(^1B)$ states and from there undergoing dissociation via the $CO_2(^3A)$ or $CO_2(^3B)$ states. Unfortunately, no data is provided for the transitions of highly vibrationally excited CO_2 [5,32,33], thus precluding the ability to accurately simulate the spectra of $CO_2(^1B)$ from first principles at a given *T*. An exception to this is the work of Malerich and Scanlon, who used an harmonic oscillator approximation to obtain Franck-Condon factors for the $CO_2(^1B) \rightarrow CO_2$ transitions to simulate spectra up to 900 K [34]. Since the validity of such an approximation towards higher temperatures and more highly vibrationally excited $CO_2(^1B)$ is questionable; we take an empirical approach where CO flame band spectra are obtained over a wide range of gas temperatures. To this end, spatially resolved afterglow spectra are obtained from inverse Abel transforms of line-of-sight spectra at the exact locations a gas temperature is measured via laser-based rotational Raman scattering.

It has been observed that over small wavelength intervals the rate coefficient for photon emission k_γ can be described by an Arrhenius form [23,35], thus a wavelength-dependent emission intensity can be defined as:

$$I_\gamma^\lambda = \kappa_\gamma^\lambda(T)[\mathrm{CO}][\mathrm{O}] \text{ and} \tag{3}$$

$$\kappa_\gamma^\lambda(T) = \kappa_0^\lambda e^{-\frac{E_a^\lambda}{T}}, \tag{4}$$

with units of photons.m^{-3}s^{-1}nm^{-1} and photons.m^{3}s^{-1}nm^{-1} respectively. The superscript λ indicates a discrete wavelength interval and κ_0^λ and E_a^λ a wavelength-dependent pre-factor and activation energy respectively.

Obtaining values for κ_0^λ and E_a^λ from measured spectra not only requires knowledge of *T*, but also of the [CO] and [O] densities. To circumvent this, we rely on the rate coefficient for the wavelength-integrated emission intensity

$$[\mathrm{CO}][\mathrm{O}] = \frac{I_\gamma}{k_\gamma(T)}, \tag{5}$$

which simultaneously ensures that the wavelength-dependent components add up to the wavelength-dependent rate coefficient:

$$k_\gamma(T) = \sum_\lambda \kappa_0^\lambda e^{-\frac{E_a^\lambda}{T}} \Delta\lambda, \tag{6}$$

with $\Delta\lambda$ as the wavelength interval. For both Eqs. (5) and (6) the wavelength range appropriate to the literature value of $k_\gamma(T)$ is used. A full error propagation is included in the final results for κ_0^λ and E_a^λ presented below, including the relative errors in absolute calibration of the spectrometer from repeated wavelength-dependent calibrations, spectrometer signal noise, estimated errors in the inverse Abel transform applied to the as-measured line-of-sight spectra, and measurement errors in the [CO][O] values obtained via Eq. (5). For the latter, this includes the measurement error in I_γ and the measurement error in *T* obtained via rotational Raman scattering. The systematic error arising from our chosen values of k_γ is not included.

3. Experimental setup

The experimental setup consists of a microwave source, a vortex flow reactor, laser scattering diagnostics, and parabolic mirror optics, as shown schematically in Figure 3.

3.1 Microwave plasma reactor

Microwaves are generated using a cavity magnetron source operated in continuous mode, producing radiation at 2.45 GHz. The magnetron has an adjustable power between 200 - 1400 W. The microwave radiation is coupled to a rectangular WR-340 waveguide via a three stub tuner. Manual tuning of the stubs ensures near-perfect matching to the plasma load, with reflected power losses < 3%.

A quartz tube (30 mm outer diameter, 27 mm inner diameter, and 400 mm length), acting as a microwave-transparent flow reactor, is inserted perpendicularly through the waveguide. The waveguide is short-circuited with a movable plunger at a quarter wavelength distance from the center of the tube, such that a standing wave is sustained in the cavity with the maximum electric field at the center of the quartz tube. A CO_2 gas flow between 6 – 12 slm is injected into the quartz tube via two 3 mm inner diameter nozzles. These nozzles are fitted tangentially and off-centered to the tube axis so that the resulting flow inside the quartz tube consists of an outer vortex spiraling to the downstream

region, with the inner regions of the tube subjected to an induced secondary vortex. This plasma-sustaining region is dominated by an upward flow, circulating back towards the injection nozzles [21,36]. The quartz tube, and surrounding vacuum components, are pumped using dry pumps in combination with a needle valve, allowing for an operating pressure between 7 mbar (ignition pressure of the plasma) and 1000 mbar. A more detailed treatment of the microwave reactor can be found in [37].

3.2 Raman scattering

A frequency-doubled laser (λ = 532 nm, Spectra-Physics GCR 230) operated at 5 W and 10 Hz is used for the laser Raman scattering, see Figure 3(a). The beam is first enlarged by a factor 4 using a telescope (not shown in Figure 3) and is then focused 4 cm upstream of the center of the plasma with an f = 2 m lens, where afterglow emission is dominant. Enlargement of the laser beam using the telescope ensures that the beam focusing at the measurement point can be approximated well with linear optics. Light scattered by the gas is collected perpendicularly to the laser beam with an achromatic doublet with f = 100 mm. A 1:1 image is projected onto a fiber bundle (27 x 400 µm) that is used to illuminate a custom-built Littrow spectrometer (f = 1 m, lens diameter d = 100 mm, $f\#$ = f/d = 10, dispersion of 0:85 nm/mm), equipped with an iCCD (Princeton Instruments PiMax 4). A long-pass filter with a cutoff wavelength of 550 nm (ThorLabs FGL550) is placed in front of the collection fibers to block scattered light at the laser wavelength from entering the spectrometer. In other words, only light that loses energy upon scattering is measured (*i.e.* the Stokes branch).

The reactor is mounted on a linear stage, which allows for lateral translation with respect to the probe laser beam, making radial scans possible. Rotational Raman spectra are measured with < 1 mm radial resolution, determined by the beam waist. More details regarding this setup can be found in [38].

Integration times on the order of 30 minutes, in combination with maximum intensification, are used to produce spectra that are fitted for each fiber individually, with only rotational temperature (T_{rot}) as a fitting parameter. Details for the spectrum fitting approach can be found in [15]. Rotational temperature as a function of fiber number (*i.e.*, axial position in the quartz tube) can be fitted well to an exponential decay function, providing a check on outliers in the data and reducing the measurement error for T to 5% – 10% in most cases.

3.3 Flame band mirror optics

Afterglow emission was measured via two parabolic mirrors (Thorlabs MPD129-F01) in combination with a USB spectrometer (Thorlabs Flame-S), see Figure 3(b). The first mirror has its 90° off-axis focus (f = 2”) placed at the same location as the Raman laser scattering setup. The resulting parallel beam is focused onto an optical fiber using a second, identical mirror. In the path of the parallel beam between the mirrors, an iris is placed with an opening of 6.9 mm, so that the solid angle for light collection is set at $\Omega = 1.45 \cdot 10^{-2}$ sr. With this low solid angle, measurements are effectively line-of-sight along a 200 µm diameter cylindrical region through the quartz tube. If measurements are performed as a function of radial position in the quartz tube, discrete inverse Abel transforms are performed using the formalism described in [39].

Using parabolic mirrors instead of lenses ensures no chromatic aberration occurs over the broad wavelength range being measured. Moreover, UV enhanced aluminum was used as a mirror coating, providing 85 - 95% reflectance between 240 - 700 nm. The spectrometer utilizes a 600 lines/mm grating blazed at 300 nm, providing an efficiency between 30 – 70% over the wavelength range of interest. A 20 cm, 200 µm, multimode UV fiber is used to minimize losses in the UV between mirror optics and spectrometer. The spectrometer was fitted with a 200 µm entrance slit, so that all light from

the fiber is coupled into the spectrometer, at the expense of a low spectral resolution of 8 nm. In order to enhance signal-to-noise further, spectra are binned over 10 nm intervals (combining the output of 22 pixels).

Absolute calibration of the quartz tube wall + mirror optics + spectrometer using D_2 (240 – 400 nm) and halogen lamps (400 – 700 nm) found a minimum sensitivity of $2.4 \cdot 10^{-8}$ μJ/count (or $2.9 \cdot 10^{4}$ photons/count) at 240 ± 5 nm and a maximum sensitivity of $1.2 \cdot 10^{-9}$ μJ/count (or $3.0 \cdot 10^{3}$ photons/count) at 500 ± 5 nm. All spectra presented in this work, including normalized spectra in arbitrary units, are based on calibrated intensities in units of photons/nm/m^2 (line-of-sight spectra) or photons/nm/m^3 (Abel-inverted spectra).

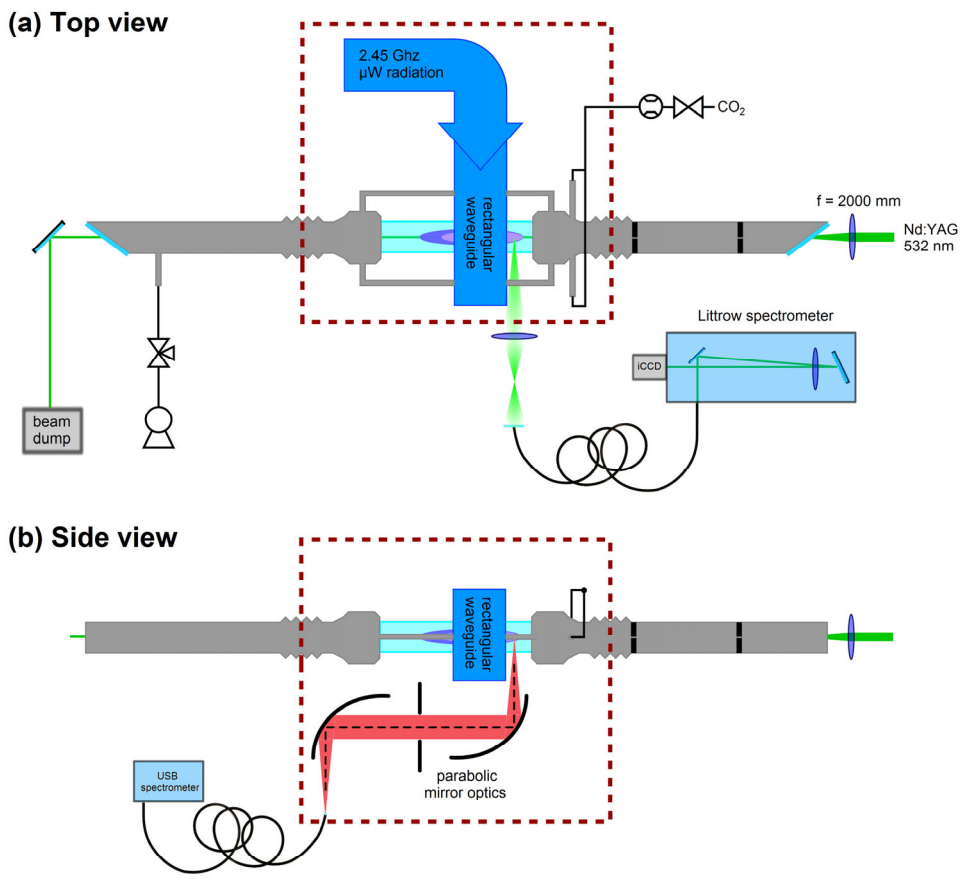

Figure 3: *Schematic (a) top and (b) side views of the microwave plasma reactor used for obtaining CO flame band spectra and independent temperature measurements via rotational Raman scattering. In this reactor, the laser + Raman collection optics and the CO flame band optics are focused on the same location in the afterglow region, which remains fixed. To obtain data in the radial direction, the waveguide + quartz tube assembly is moved up or down along the page in the top view.*

4. Results & Discussion

4.1 Constructing an empirical model for CO flame bands

Two radial scans of (line-of-sight integrated) CO flame band spectra and (local) rotational Raman spectra were collected 4 cm from the center of the plasma (2 cm into the afterglow above the waveguide) at input powers of 330 W and 1000 W, pressures 200 mbar and 260 mbar, and input flow

rates of CO_2 of 7 slm and 8 slm. The CO flame band spectra were subsequently Abel-inverted to obtain local spectra. The resulting CO flame band spectra are shown in Figure 4, where they are normalized to their maximum intensity values to allow for an easy comparison of the spectrum shape. As can be seen in Figure 4, there is a clear shift of the intensity maximum with increasing temperature, an effect previously observed by Slack & Grillo in spectra obtained at 1300 K and 2700 K [23].

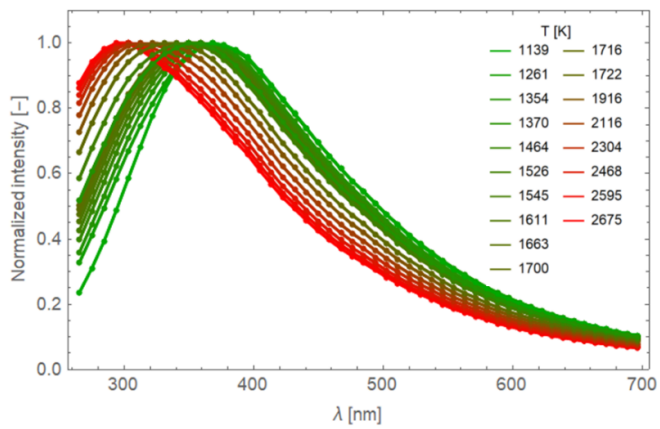

Figure 4: *Abel-inverted afterglow spectra normalized at their maximum intensity values. Gas temperatures T indicated in the legend are obtained from rotational Raman scattering. A clear shift towards shorter wavelengths is observed with increasing gas temperature.*

With the gas temperatures known through the use of rotational Raman scattering, Eq. (5) was used to obtain the product [CO][O] for all conditions, so that the intensity data I_γ^λ could be corrected to rate coefficients κ_γ^λ in units of photons.m^{3}s^{-1}nm^{-1} at every wavelength. All available data was then used to create Arrhenius plots at wavelengths between 265 nm and 700 nm, in steps of approximately 10 nm. Examples of these Arrhenius plots, including fits to Eq. (4), are depicted in Figure 5. As seen in this figure, κ_γ^λ follows the Arrhenius-type behavior within the measurement error at all wavelengths. The only substantial deviations occur at wavelengths below 300 nm, with a typical example at λ = 265 nm shown in Figure 5(a).

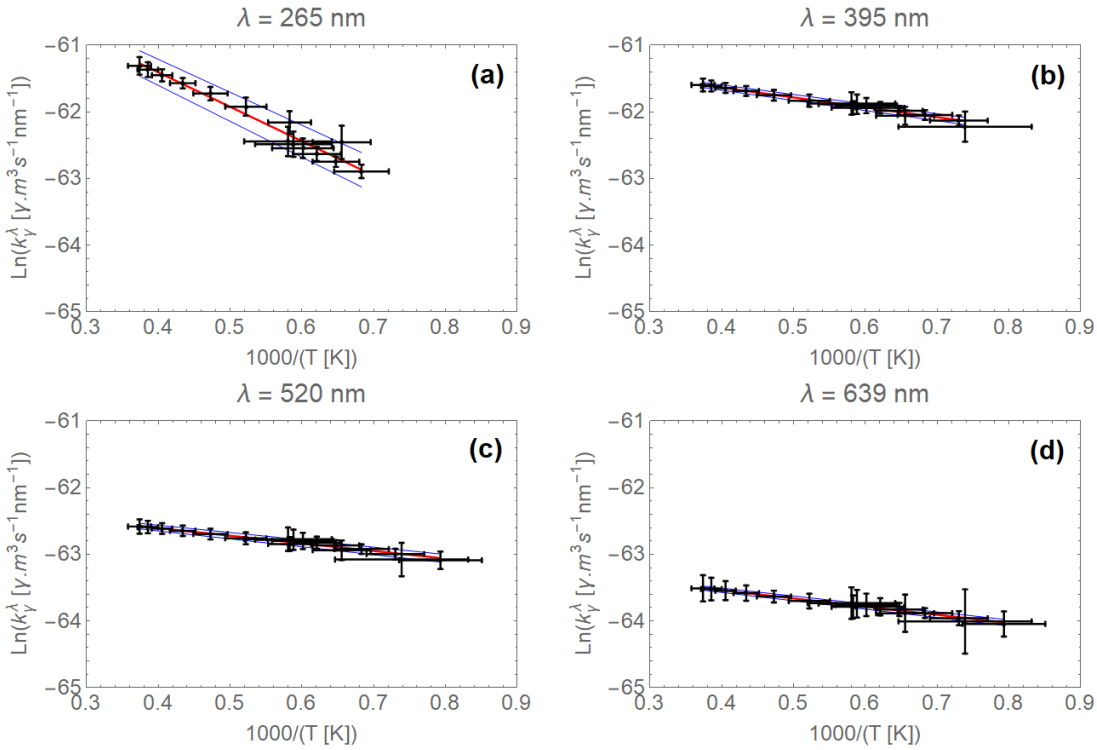

Figure 5: *Wavelength- dependent Arrhenius fits at four selected wavelength intervals. For the measured data, error bars in the vertical direction include (relative) errors in absolute calibration of the spectrometer, spectrometer signal noise, estimated errors in the Abel inversion and errors in the [CO][O] values used to calibrate the data. Error bars in the horizontal direction indicate the error in the rotational Raman temperature measurements. The central straight line (red) is the least-squared fit, with the blue straight lines indicating the extrema of the fit based on the 1-σ error of the two fitted parameters* κ_0^λ *and* E_a^λ.

The sizable horizontal error bars at lower *T* in Figure 5 are a consequence of scatter in repeated rotational Raman spectra at a given position and measurement condition. While Raman spectra can be obtained with higher signal-to-noise at lower *T* (and thus, higher neutral gas density), the lower *T* points are found near the edge of the quartz tube. Near the tube edge, however, vortex flow instabilities can lead to shifts in temperature during accumulation of spectra. In the UV, such as in Figure 5(a), the lower *T* points are missing as a direct consequence of the $CO_2(^1B)$ emission being well below the detection limit of the optical system at these wavelengths.

Results for Arrhenius pre-factors κ_0^λ and activation energies E_a^λ from the error-weighted linear regressions in Figure 5 are shown in Figure 6(a,b). Here it becomes evident that both κ_0^λ and E_a^λ increase towards the UV, with E_a^λ mostly leveling off for λ > 450 nm. Note that while values for κ_0^λ depend on the choice of $k_\gamma(T)$, activation energies E_a^λ are absolute and depend directly on the measured rotational Raman temperatures.

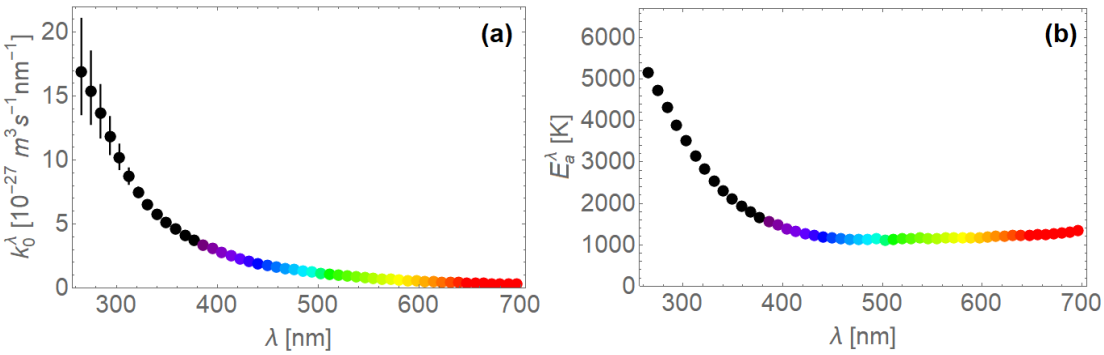

Figure 6: *Wavelength-dependent Arrhenius coefficients κ_0^λ and E_a^λ. Error bars are indicated, but for E_a^λ fall within the point size. Colors indicate the visible spectrum. All data points are tabulated in the Supplementary Information.*

At λ > 400 nm, E_a^λ is relatively constant at 1100 K (or 0.09 eV), less than the wavelength-averaged activation energy of 2080 K (or 0.18 eV) assumed for k_γ. From the relation between the overall recombination rate coefficient k_{rec} and k_γ in Eq. (2), the only difference in activation energies between these two rate coefficients comes from the activation energy for quenching of the $CO_2(^1B)$ state via R3, which itself might depend on wavelength (or, more accurately, the internal state of $CO_2(^1B)$). Figure 5 perfectly illustrates why determinations of k_{rec} from CO flame bands lead to lower activation energies for R5 at low *T* (where only emission > 300 nm can be distinguished) than in similar experiments performed at higher *T*, see *e.g.* [23,30]. Rate coefficients for k_{rec} from more absolute measurement techniques are preferred, with comparison to k_γ at best providing some insight into the quenching behavior: taking the commonly used activation energy of 1510 K for k_{rec} from Tsang & Hampson [26], we can conclude that quenching of $CO_2(^1B)$ at λ > 400 nm has an activation energy of ~ 400 K.

The pre-factor k_0^λ fits very well to a power law:

$$k_0^\lambda \approx 2.78 \cdot 10^{-16} \cdot \lambda^{-4.21}. \tag{7}$$

Part of this rapid increase of pre-factor at shorter wavelengths may be accounted for by a decrease in the natural radiative lifetime in R4 at higher energies. Since the time between molecular collisions at the conditions used here is approximately 2 ns, and the natural radiative lifetime of the $CO_2(^1B)$ state is at least 200 ns [3,30], full thermalization of this state is expected to occur prior to reaction R4. With the final state of $CO_2(^1B)$ from which photon emission occurs not depending strongly on its history via reactions R1 and R2, the most likely candidate for affecting k_0^λ is the quenching reaction R3. A strong reduction in the probability for R3 with $CO_2(^1B, v_1 = v_2 = v_3 > 0)$ would translate to a substantial increase in k_0^λ at shorter wavelengths.

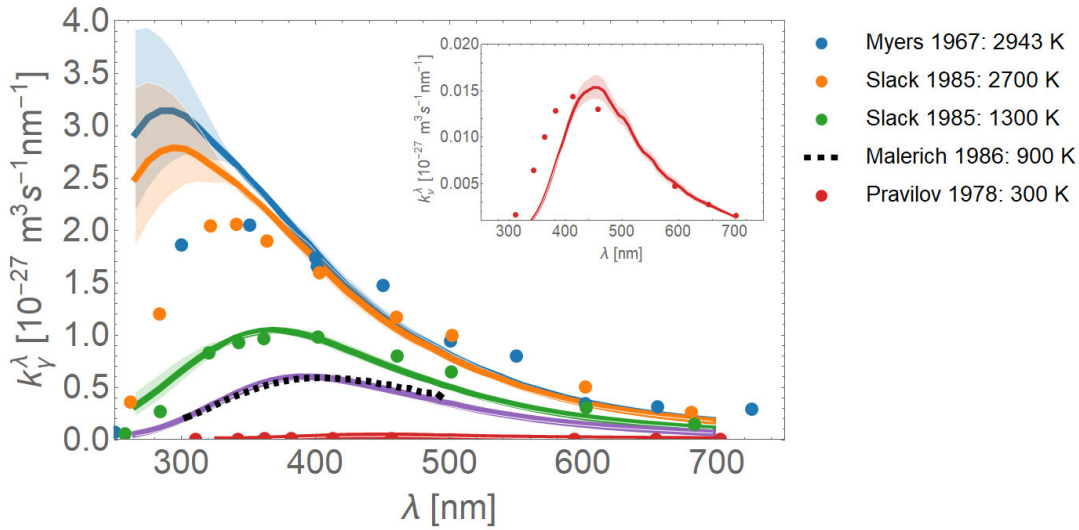

Figure 7: *Wavelength-dependent rate coefficients κ_γ^λ derived in this work (solid lines) compared to literature sources (points, with the dashed line for Malerich indicating a simulated spectrum)* [3,4,23,34]. *The inset shows a zoom on the Pravilov comparison at 300 K. Note that Myers, Malerich and Pravilov data extend beyond the temperature range investigated in this work by + 300 K, - 200 K and - 840 K respectively, so that the solid lines represent extrapolations.*

4.2 Comparison of the empirical model to literature

An alternative interpretation for results of κ_0^λ and E_a^λ at λ < 400 nm becomes necessary after comparison to previously measured κ_γ^λ data in Figure 7. The correspondence at λ > 400 nm is very reasonable, and the approximate spectral simulation by Malerich & Scanlon matches very well with the empirical model employed here, despite the latter being extrapolated by 200 K below the minimum measured temperature [34]. The extrapolation is still accurate when extended down to 300 K, as shown in the inset of Figure 7. It is worth noting that if our empirical model is produced based on data obtained only at 200 mbar (and neglecting the higher temperature data obtained at 260 mbar), the correspondence with the 300 K data obtained by Pravilov & Smirnova is further improved [3]. This serves to indicate that our empirical model for κ_γ^λ could be further refined with the inclusion of lower temperatures. The most significant deviation between the current work and literature data occurs in the UV region at higher *T*: our data predicts a much higher UV component. The most significant differences between the current work and that of Myers & Bartle [4] and Slack & Grillo [23] are:

(i) our proximity to an active plasma, a potential source of additional excited species,
(ii) their use of shock tubes operated at peak pressures of 1.5 – 3.0 bar to obtain high peak temperatures and subsequent dissociation of O_2 or O_3 to atomic O, and
(iii) their typical gas composition of CO_2:CO:O:O_2:Ar ≈ 10:10:1:1:78, while at the highest temperatures measured here the estimated composition of the afterglow is CO_2:CO:O:O_2:Ar ≈ 60:25:5:10:0 [21].

Regarding (i), the estimated time-of-flight to the measurement location 2 cm away from the plasma is 1 – 2 ms, so that at best metastable excited species will survive. However, with predominantly CO and O emerging from the plasma, no obvious candidate metastable species leading to emission further

downstream present themselves. Similarly, ion densities are likely far too low to lead to significant rates of radiative ion-electron recombination reactions. This conclusion is supported by the fact that at lower *T* the afterglow spectra from plasma are almost equal to spectra obtained in the thermal flame and shock tube conditions depicted in Figure 7.

For (ii), it may be reasonable to expect that the much higher pressures employed by Myers & Bartle and Slack & Grillo lead to proportionally more quenching of highly excited $CO_2(^1B, \nu_1 = \nu_2 = \nu_3 > 0)$ so that the UV component is strongly reduced. As discussed previously, the time between collisions is already significantly shorter than the natural radiative lifetime of the excited state at our reduced pressures [3,30], therefore, we do not consider this a sufficient explanation.

Regarding (iii), both authors determine that O_2 does not lead to significant *additional* quenching. However, an alternative mechanism is suggested by Myers & Bartle [4], as well as by Pravilov & Smirnova [30]:

$$CO_2(^1B) + O_2 \rightarrow CO_2 + O_2(^3B), \tag{R6}$$

$$O_2(^3B) + M \rightarrow O_2 + M \text{ and} \tag{R7}$$

$$O_2(^3B) \rightarrow O_2 + h\nu \tag{R8}$$

where R8 leads to emission of O_2 Schumann-Runge bands between 180 – 450 nm. Referring back to Figure 1, exchange of energy between $CO_2(^1B)$ and O_2 is quite likely considering the overlap in potential energy between $CO_2(^1B)$ and $O_2(^3B)$. Energy levels close to resonance might exist between these two states, allowing for reaction R6 to proceed at a sufficient rate. Comparing the difference between our result and the experiment of Myers & Bartle, we indeed find a good correspondence with the O_2 Schumann-Runge bands, see Figure 8. When calculating the expected emission based on R1 – R8 we find (see the Supplementary Information for a derivation):

$$I_\gamma^{O_2} \approx \frac{k_6^+ k_8^+}{k_4^+ k_7^+} \mathcal{X}_{O_2} \cdot I_\gamma \propto \mathcal{X}_{O_2} \cdot [\mathrm{CO}][\mathrm{O}], \tag{8}$$

revealing that this mechanism is (a) proportional to the molecular oxygen fraction $\mathcal{X}_{O_2}$ and (b) proportional to CO + O flame band emission I_γ. Because our O_2 concentration is expected to be significantly higher than in the shock tube experiments, the mechanism of R6 - R7 would produce far more O_2 Schumann-Runge emission. Furthermore, since it would scale directly with [CO][O], it is not easily distinguished in the Arrhenius plots of Figure 5, and does not lead to significant discontinuities in the values of κ_a^λ and E_a^λ as a function of wavelength. The small offsets observed at λ < 300 nm, such as in Figure 5(a), may be caused by differences in $\mathcal{X}_{O_2}$ at the different measurement positions, however.

Another channel for the emergence of O_2 Schumann-Runge emission occurs via the recombination of atomic oxygen in the electronic ground-state leading to the overall reaction:

$$O + O \rightarrow O_2(^3B) + h\nu. \tag{R9}$$

This chemiluminescent process has been shown to have a high activation energy of ~ 14000 K and can account for at most 20% of the observed UV radiation [4,40,41]. If this process were dominant in the production of O_2 Schumann-Runge emission, it would reveal itself by a much greater increase in

E_a^λ towards lower wavelengths in Figure 6 than is currently observed. Therefore, it can be concluded that reaction chain R6 - R8 is the probable origin of the excess UV emission.

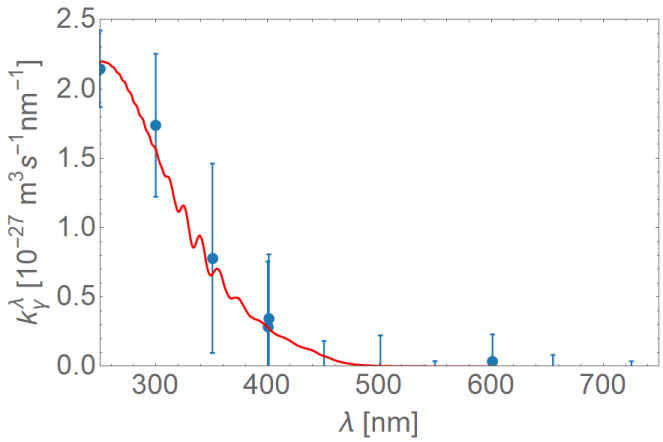

Figure 8: *The difference between our model and the data of Myers & Bartle* [4] *(points) to a simulated O_2 Schumann-Runge spectrum at $T = T_{rot} = T_{vib} = 2943$ K (solid line). The error bars indicate only the measurement error from Myers & Bartle.*

A definitive analysis of the UV emission at increased temperature will require a high resolution study of the spectrum to identify individual transitions. Combined with our recent development of obtaining a direct measurement of [CO], [O] and [O_2] from rotational Raman data [19], the contributions of $I_\gamma^{O_2}$ in Eq. (8) and I_γ in Eq. (3) to the total spectrum can be disentangled. Based on current data, we argue that our results are representative of CO flame band emission up to temperatures of at least 1500 K. At higher temperatures the unknown atomic and molecular oxygen fractions may lead to deviations of the Arrhenius model based on the coefficients in Figure 6.

4.3 Application of the CO flame band Arrhenius model: elucidating post-plasma cooling

As a demonstration of our proposed method, we apply the Arrhenius model on the microwave plasma reactor depicted in Figure 2 at operating conditions close to the original measurements on which the empirical model is based. Line-of-sight spectra were obtained along the width of the tube every 1 mm and along the length of the tube every 1 cm. After applying the Abel inversion to the spectra obtained along the width of the tube (forcing symmetry in the radial direction), the Arrhenius model was fitted to the spectra, and a temperature obtained (see the Supplementary Information for example fits). Resulting temperature maps for locations downstream of the plasma are depicted in Figure 9, at plasma powers of 860 W and 1300 W, pressures of 100 mbar and 300 mbar and CO_2 input flows of 6 and 12 slm. Residuals of the Arrhenius model fits to the measured spectra are < 5% at all wavelengths and all positions for this data, including those for the 300 mbar, 6 slm data where the maximum fitted temperature is 1950 K. At this position there is already significant UV emission at λ = 260 nm, indicative of the O_2 Schumann-Runge emission discussed above. Considering that the quality of the fit is not adversely affected, we tentatively conclude that $\mathcal{X}_{O_2}$ depends only on *T* and not on *e.g.* pressure or time-of-flight of species from the plasma. The quality of the fit *is* adversely affected for spectra obtained closer to the plasma at 300 mbar, such as exactly to the side of the (~ 3 mm wide) plasma within the waveguide, where gas temperature may increase to > 3000 K [20]. Results for these

positions are therefore not included here, with future work aiming to extend our understanding of afterglows in pure CO_2 plasma towards higher temperatures.

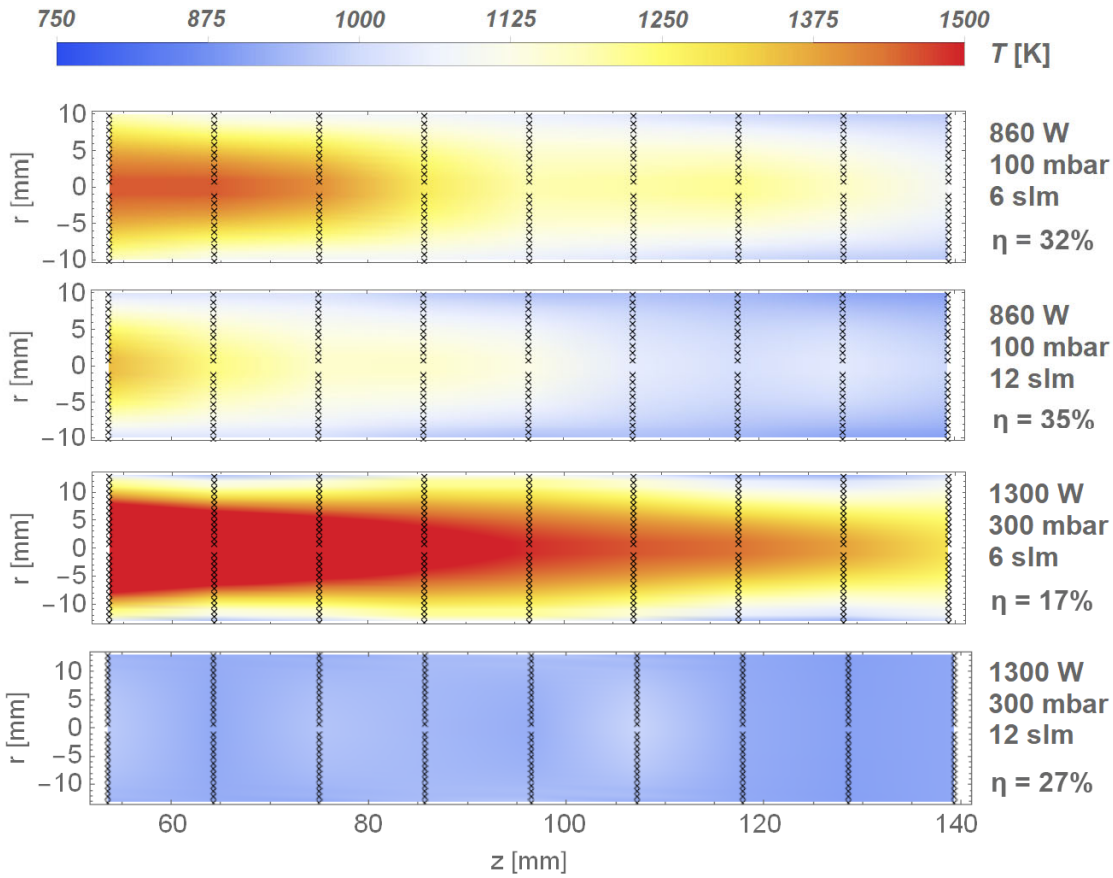

Figure 9: *Example temperature maps in the afterglow. Maximum T for the 300 mbar, 6 slm data is 1950 K. Crosses indicate the original measurement positions. The coordinates on the horizontal axis increase in the downstream direction, with z = 0 mm located at the center of the waveguide (coinciding with the approximate center of the plasma; the bottom edge of the plasma is located at z ≈ 20 mm). The residuals of the Arrhenius model fits to the measured spectra are < 5% at all wavelengths and all positions for this data. Energy efficiency η for CO creation for each condition is also indicated.*

4.3.1 CO losses and heat generated in the downstream region

Analyzing the temperature maps of Figure 9 for the region at least 3 cm downstream of the plasma (z > 53 mm), we observe that the decrease of T along the length of the tube depends strongly on flow and pressure. Both a reduction in pressure and an increase in flow rate imply a shorter time-of-flight from the bottom end of the plasma to the measured positions in Figure 9. The peak temperature in the plasma is ~ 3500 K at 100 mbar and ~ 6000 K at 300 mbar, irrespective of flow rate [20,21]. Nonetheless, we observe much lower temperatures in the downstream region at 12 slm versus 6 slm for both pressures. The effect of doubling the flow is also more significant for the 300 mbar data. The highest energy efficiencies η for the complete CO_2 conversion process, also indicated in Figure 9, coincide with temperatures already being below 1500 K at 3 cm below the plasma. Losses of CO within the afterglow region covered in Figure 9 can be evaluated as follows:

$$\rho_{CO+O} = k_{rec}(T)[\mathrm{CO}][\mathrm{O}][\mathrm{M}] \cdot \Delta\mathrm{H}_{\mathrm{CO+O}}(T), \tag{9}$$

where ρ_{CO+O} is the heat production in W/m^3 from CO + O recombination via R5, $k_{rec} = 1.7 \cdot 10^{-45} e^{-\frac{1510}{T}}$ m^{6}s^{-1} the rate coefficient for this reaction via Tsang & Hampson [26], the product [CO][O] in m^6 as obtained from the integrated emission intensity I_γ via Eq. (3) and $\Delta H_{\mathrm{CO+O}}(T)$ the change in enthalpy for this reaction in *J*. The results of applying Eq. (9) to our data in Figure 9 are shown in Figure 10 for the two 6 slm conditions, which can be expected to have the most recombination. Integrating ρ_{CO+O} over the measured region (in cylindrical coordinates) provides the heat generated in the afterglow from CO + O reactions: 2.2 W at 100 mbar and 48 W at 300 mbar. Though certainly a negligible loss at 100 mbar, at 300 mbar this equates to a loss of ~ 10% of CO molecules along the length of the tube within the measured region. Improved quenching in this region would therefore allow for a modest increase of *η* from 17% to 19%.

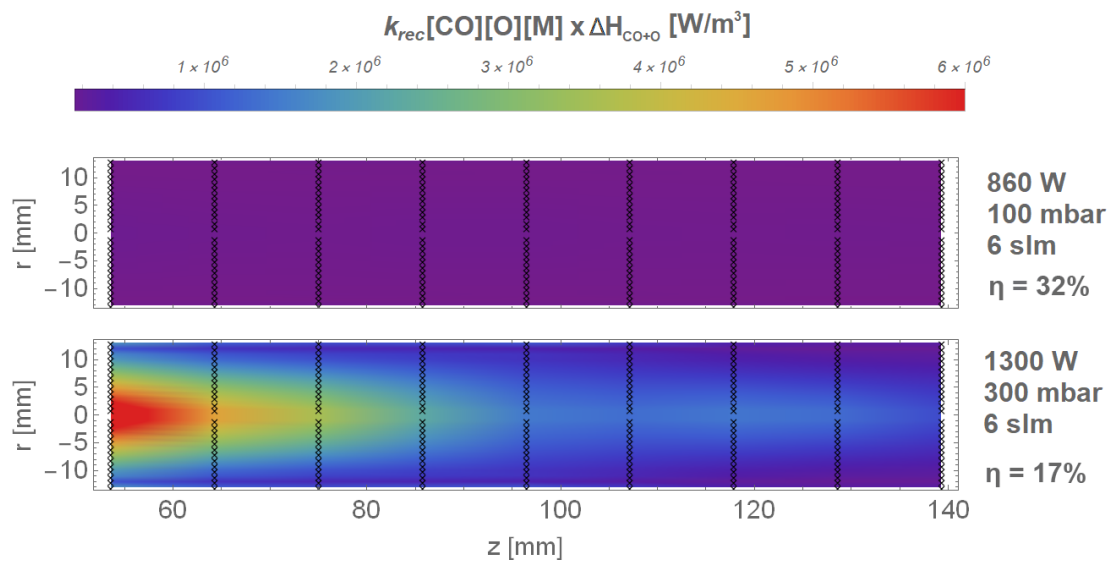

Figure 10: *Heat production from CO + O recombination at two conditions: at 100 mbar data, only 2.2 W is lost within the measured region, and at 300 mbar just 48 W is lost via this channel.*

4.3.2 Estimated atomic O molar fractions and re-heating at increased pressure

With CO losses via R5 along the length of the tube deemed negligible, other estimates can be made using the CO flame band data. Given that the [CO][O] product and *T* are known, and the CO content in the gas stream is not expected to change significantly at *z* > 53 mm, an estimate for [O] can be extracted. In Table 1, the CO molar fraction $\mathcal{X}_{\mathrm{CO,final}}$ measured far downstream using mass spectrometry [21] is used to divide the molar fraction product $\overline{\mathcal{X}_{\mathrm{CO}} \cdot \mathcal{X}_{\mathrm{O_{start}}}} = [\mathrm{CO}][\mathrm{O}]/n_0^2$ and obtain an estimate of the atomic O molar fraction $\overline{\mathcal{X}_{\mathrm{O_{start,est}}}}$ at z = 53 mm in Figure 9. Clearly, atomic O molar fractions are at most ~ 1%, with almost no atomic O present at 300 mbar and 12 slm. At 300 mbar atomic O recombination via

$$\mathrm{O + O + M \rightarrow O_2 + M} \qquad \text{(R10)}$$

undoubtedly proceeds at a higher rate compared to 100 mbar. R10 lacks an activation energy and its rate is, therefore, not significantly enhanced with increasing *T*. The highest atomic O concentrations present also at 300 mbar, but at 6 slm, implies that additional production of atomic O occurs between plasma and *z* = 53 mm. The likely contender for this process is

$$CO + O_2 \leftrightarrow CO_2 + O, \quad \text{(R11)}$$

which possesses an equilibrium constant of $k_8^+/k_8^- = 0.14 \cdot e^{\frac{2500}{T}}$ [26]. While the probability of R11 towards the production of O decreases with increasing *T*, the higher concentrations of O at 300 mbar, 6 slm likely result from a higher initial conversion of CO_2 to CO at the height of the plasma: the rate of R11 towards the right-hand-side is enhanced due to higher $[CO][O_2]$ compared to $[CO_2][O]$. This, in turn, leads to an increased rate for R10. In essence, an overproduction of CO at the height of the plasma is returned as a delayed re-heating of the gas stream downstream. This is why, in Figure 9, the temperatures are significantly higher at 300 mbar, 6 slm, compared to 300 mbar, 12 slm, despite the former having had a longer time-of-flight from the bottom of the plasma.

Table 1: *Estimated radial mean atomic O concentrations* $\overline{\mathcal{X}_{\mathrm{O}}}_{start,est}$ *at z = 53 mm for the conditions of Figure 9.* $\mathcal{X}_{CO,final}$ *is based on mass spectrometry ~ 2 m downstream of the plasma* [21] *and* $\overline{\mathcal{X}_{\mathrm{CO}} \cdot \mathcal{X}_{\mathrm{O}}}_{\mathrm{start}}$ *is derived from the radial mean of afterglow emission intensity* I_γ *at z = 53 mm,* $\overline{\mathcal{X}_{\mathrm{O}}}_{start,est}$ *is obtained assuming* $\mathcal{X}_{CO,final} \approx \mathcal{X}_{CO,start}$.

p [mbar]	*P* [W]	*Flow* [slm]	*SEI* [eV/molecule]	$\mathcal{X}_{\mathrm{CO,final}}$ [-]	$\overline{\mathcal{X}_{\mathrm{CO}} \cdot \mathcal{X}_{\mathrm{O}}}_{start}$ [-]	$\overline{\mathcal{X}_{\mathrm{O}}}_{start,est}$ [-]
100	860	6	2.0	0.20	$1.1 \cdot 10^{-3}$	$5.5 \cdot 10^{-3}$
100	860	12	1.0	0.11	$0.68 \cdot 10^{-3}$	$6.3 \cdot 10^{-3}$
300	1300	6	3.0	0.16	$0.21 \cdot 10^{-3}$	$13 \cdot 10^{-3}$
300	1300	12	1.5	0.13	$6.4 \cdot 10^{-7}$	$4.8 \cdot 10^{-6}$

4.3.3 Heat lost to the environment in the early afterglow

With gas compositions relatively stable at $z \geq 53$ mm and assumed to consist mainly of CO_2, CO and O_2, and temperatures at the start of the measured afterglows known, the heat lost between plasma and *z* = 53 mm can be estimated. Here, it is assumed that the mass flow profile along the width of the tube is flat, as calculated using Ansys Fluent in [21]. Combining the enthalpy for CO_2, CO and O_2 as a function of temperature with the CO and O_2 concentrations based on $\mathcal{X}_{CO,final}$, the power contained within the flow at *z* = 53 mm is calculated. Table 2 lists the total power, P_{total}, the power contained in chemical enthalpy, P_{chem}, and the power contained in heat, P_{heat}. One additional parameter is estimated: the fraction of the heat generated in the plasma that was already released to the environment prior to *z* = 53 mm. To obtain this fraction, it is assumed that at the height of the plasma 60% of the input power *P* goes towards heating the gas and 40% towards CO_2 dissociation, calculated using the CO_2 plasma reactor model in [21]. Comparing the numbers in Table 2, higher flow rates still contain more power at *z* = 53 mm than lower flow rates. This is especially apparent for the 100 mbar, 12 slm condition, where very little of the initial 860 W has been lost to the environment. This is again reflected in the 27% fraction of heat lost, which for all other conditions is above 70%. Since this remarkable difference coincides with the 100 mbar, 12 slm condition having the highest energy efficiency of η = 35%, this implies that removing heat from the system too fast may reduce the formation of CO. This conclusion is based on the fact that at this condition $\bar{T}_{start}$ = 1260 K is already below the level required to freeze in CO, while most of the heat in the gas is still to be removed from the system; thus, between plasma and *z* = 53 mm a region of optimal composition and temperature must exist that maximizes CO and minimizes *T* (*i.e.* maximizing η). The chemistry in this region could be elucidated further once our method for afterglow analysis is extended towards higher temperatures and variable gas compositions.

Table 2: *Radial mean gas temperatures $\overline{T}_{start}$ at z = 53 mm, power contained within the flow at z = 53 mm, P_{total}, its subdivision into power contained in chemical enthalpy, P_{chem}, and heat, P_{heat}, and the fraction of heat already cooled away at z < 53 mm. The latter assumes 40% of the input power P initially goes towards chemistry and 60% towards heating the gas* [21].

p [mbar]	*P* [W]	*Flow* [slm]	*SEI* [eV/molecule]	$\overline{T}_{start}$ [K]	P_{total} [W]	P_{chem} [W]	P_{heat} [W]	Fraction of heat lost at z < 53 mm [%]
100	860	6	2.0	1120	445	274	171	0.71
100	860	12	1.0	1260	711	299	412	0.27
300	1300	6	3.0	1507	480	211	269	0.75
300	1300	12	1.5	993	627	347	280	0.71

5. Summary & Conclusions

We have investigated CO flame band emission ($CO + O \rightarrow CO_2 + h\nu$) in pure CO_2 microwave plasma by obtaining absolute emission spectra at various locations in the plasma afterglow while simultaneously measuring gas temperatures using rotational Raman scattering. An empirical model for simulating these spectra was constructed by fitting the Arrhenius equation to the absolute emission as a function of gas temperature at various wavelengths between 260 – 700 nm. With the spectrum shape depending strongly on gas temperature, a method for easily obtaining gas temperatures surrounding the plasma is obtained.

Comparison of our results to literature for CO flame band emission obtained in CO/O_2 flames and shock tubes reveal a much stronger UV component emerging in our spectra at temperatures > 1500 K. This UV component is consistent with O_2 Schumann-Runge emission and likely results from the collisional exchange of internal energy between $CO_2(^1B)$ and O_2. Thus, with the UV component dependent on the O_2 fraction in the gas, our empirical model for afterglow emission cannot be directly applied at all conditions. In a follow-up study, the composition of the gas will be measured in addition to the absolute emission spectra by using a new rotational Raman scattering technique [19], allowing for reliable extension of the afterglow emission model to higher temperatures.

To demonstrate our method, afterglow emission starting at ~ 3 cm downstream of the CO_2 microwave plasma is analyzed, where temperatures are sufficiently low to apply the current empirical model. The resulting temperature maps showed large variations in the distribution of gas temperature with pressure and flow rate. The amount of heat generated through $CO + O + M \rightarrow CO_2 + M$ was calculated as 2.2 W at 860 W, 100 mbar, 6 slm and 48 W at 1300 W, 300 mbar, 6 slm. Since this represents a negligible loss of CO, measurements of CO densities further downstream could be used to evaluate compositions at ~ 3 cm from the plasma. This analysis revealed < 1% atomic O for all conditions, with the highest pressure and lowest flow rates (300 mbar, 6 slm) maintaining the most atomic O towards the downstream region. We argue that this maximizing of atomic O results from an overproduction of CO at the height of the plasma, thus pushing the balance of the $CO + O_2 \leftrightarrow CO_2 + O$ reaction towards the right-hand-side in the early afterglow. The additional atomic O thus produced leads to additional heating downstream of the plasma after recombination to molecular O_2. This same process is seen to be avoided when doubling the flow from 6 to 12 slm, since the CO produced in the plasma becomes significantly diluted by additional CO_2 and temperatures remain significantly lower beyond ~ 3 cm downstream. The highest energy efficiency for CO production is shown to coincide with an operating

condition (860 W, 100 mbar, 12 slm) where very little heat has been lost to the environment prior to ~ 3 cm downstream. This implies that removing heat from the system as fast as possible post-plasma is not necessarily beneficial, but that a region can be formed in which an optimal composition and temperature exists that maximizes CO and minimizes *T* without significant cooling to the environment. At 860 W, 100 mbar, 12 slm, this region ends at a temperature $T \approx 1260$ K within 3 cm of the plasma; already below the level required to effectively freeze in CO and thus precluding the need for a sophisticated downstream cooling method.

Acknowledgements

The authors wish to thank B. van Hemert for designing the mirror optics assembly, T.W.H. Righart for integrating the spectrometer data acquisition with the stepper motors, A.J. Wolf for recalibrating mass spectrometry data and V. Guerra (IST Lisbon) for valuable discussions. The work of G. Raposo was supported by an Erasmus+ traineeship grant.

References

[1] Ibraguimova L B, Minaev B F and Irgibaeva I S 2014 Spin-orbit coupling and dissociation of CO2 molecules *Opt. Spectrosc.* **117** 695–702

[2] Ibraguimova L B and Minaev B F 2016 Analysis of Dissociation—Recombination Processes for the CO2 Molecule with the Spin—Orbit Coupling Taken into Account *Opt. Spectrosc.* **120** 345–51

[3] Pravilov A M and Smirnova L G 1978 Spectral Distribution of the Chemiluminescence Rate Constant in the O(3P) + CO (+ M) and O(3P) + NO (+ He) Reactions *Kinet. Catal.* **19** 902–8

[4] Myers B F and Bartle E R 1967 Shock-tube study of the radiative processes in systems containing atomic oxygen and carbon monoxide at high temperature *J. Chem. Phys.* **47** 1783–92

[5] Schmidt J A, Johnson M S and Schinke R 2013 Carbon dioxide photolysis from 150 to 210 nm: Singlet and triplet channel dynamics, UV-spectrum, and isotope effects *Proc. Natl. Acad. Sci. U. S. A.* **110** 17691–6

[6] Grebenshchikov S Y 2017 Infrared Spectra of Neutral Bent Carbon Dioxide *J. Phys. Chem. A* **121** 4296–305

[7] Kivel B, Hammerling P and Teare J D 1961 Radiation from the Non-Equilibrium Region of Normal Shocks in Oxygen, Nitrogen and Air *Planet. Space Sci.* **3** 132–7

[8] Burch J G 1885 Some Experiments on Flame *Nature* **31** 272–5

[9] Burch J G 1886 Further Experiments on Flame *Nature* **35** 165–6

[10] Weston F R 1925 The flame spectra of carbon monoxide and water-gas. —Part I *Proc. R. Soc. London. Ser. A* **109** 176–86

[11] Weston F R 1925 The flame spectra of carbon monoxide and water gas. Part II *Proc. R. Soc. London. Ser. A* **109** 523–6

[12] Fowler A and Gaydon A G 1933 Spectrum of the Afterglow of Carbon Dioxide *Proc. R. Soc. A Math. Phys. Eng. Sci.* **142** 362–9

[13] Clyne M A A and Thrush B A 1962 Mechanism of chemiluminescent combination reactions involving oxygen atoms *Proc. R. Soc. London. Ser. A. Math. Phys. Sci.* **269** 404–18

[14] Dixon R N and A P R S L 1963 The carbon monoxide flame bands *Proc. R. Soc. London. Ser. A. Math. Phys. Sci.* **275** 431–46

[15] van den Bekerom D C M, Palomares Linares J M, van Veldhuizen E M, Nijdam S, van de Sanden M C M and van Rooij G J 2018 How the alternating degeneracy in rotational Raman spectra of CO 2 and C 2 H 2 reveals the vibrational temperature *Appl. Opt.* **57** 5694

[16] Gaydon A G and Guedeney F 1955 Effect of Preheating on the Spectra of Carbon Monoxide Difusion Flames *Trans. Faraday Soc.* **51** 894–900

[17] Slack M and Grillo A 1985 High temperature rate coefficient measurements of CO + O chemiluminescence *Combust. Flame* **59** 189–96

[18] Gatti N, Ponduri S, Peeters F J J, van den Bekerom D C M, Minea T, Tossi P and van Rooij G J 2017 Assessing the non–equilibrium in N2 microwave plasma with spontaneous Raman scattering *To be Submitt.*

[19] Van de Steeg A W, Vialetto L, Silva A F, Peeters F J J, Van den Bekerom D C M, Gatti N, Diomede P, Van de Sanden M C M and Van Rooij G J 2021 Revisiting spontaneous Raman scattering for direct oxygen atom quantification *Opt. Lett.* **Accepted f**

[20] Wolf A J, Peeters F J J, Bongers W A and Sanden M C M van de 2020 Implications of thermo-chemical instability on the contracted modes in CO2 microwave plasmas *Plasma Sources Sci. Technol.* **26**

[21] Wolf A J, Peeters F J J, Groen P W C, Bongers W A and Van De Sanden M C M 2020 CO2 Conversion in Nonuniform Discharges: Disentangling Dissociation and Recombination Mechanisms *J. Phys. Chem. C* **124** 16806–19

[22] Slanger T G, Wood B J and Black G 1972 Kinetics of O(3P) +CO +M recombination *J. Chem. Phys.* **57** 271–6

[23] Slack M and Grillo A 1985 High Temperature Rate Coefficient Measurement of CO + O Chemiluminescence *Combust. Flame* **59** 189–96

[24] Brabbs T A and Belles F E 1967 Recombination of carbon monoxide and atomic oxygen at high temperatures *Symp. Combust.* **11** 125–35

[25] Stuhl F and Niki H 1971 Determination of rate constants for reactions of O atoms with C 2H2, C2D2, C2H 4, and C3H6 using a pulsed vacuum-uv photolysis-chemiluminescent method *J. Chem. Phys.* **55** 3943–53

[26] Tsang W and Hampson R F 1986 Chemical Kinetic Data base for Combustion Chemistry. Part 1. Methane and Related Compounds *J. Phys. Chem. Ref. Data* **15**

[27] Simonaitis R and Heicklen J 1972 Kinetics and mechanism of the reaction of o(3p) with carbon monoxide *J. Chem. Phys.* **56** 2004–11

[28] Pravilov A M and Smirnova L G 1981 Chemiluminscence Process in O(3P)+ CO + M System: Segregation of Heterogeneous Component and Reactions with the Participation of Impurities *Kinet. Catal.* **22** 416–9

[29] Pravilov A M and Smirnova L G 1981 The Relationship of Chemiluminscence and the Formation of CO2 in the O(3P) + CO + M System *Kinet. Catal.* **22** 90–7

[30] Pravilov A M and Smirnova L G 1981 Temperature Dependence of the Spectral Distribution of

the Rate Constant of Chemiluminescence in the Reaction O(3P) + CO -> CO2 + hv *Kinet. Catal.* **22** 641–6

[31] Baulch D L, Drysdale D D, Duxbury J and Grant S J 1976 *Evaluated Kinetic Data for High Temperature Reactions: Vol 3* (Butterworths)

[32] Grebenshchikov S Y 2013 Photodissociation of carbon dioxide in singlet valence electronic states. II. Five state absorption spectrum and vibronic assignment *J. Chem. Phys.* **138**

[33] Grebenshchikov S Y and Borrelli R 2012 Crossing electronic states in the Franck-Condon zone of carbon dioxide: A five-fold closed seam of conical and glancing intersections *J. Phys. Chem. Lett.* **3** 3223–7

[34] Malerich C J and Scanlon J H 1986 Calculation of CO + O Recombination Chemiluminescence Spectrum *Chem. Phys.* **110** 303–13

[35] Eremin A V and Ziborov V S 1993 Nonequilibrium radiation from the CO2 band (1B2-X1) in shock-heated flows *Shock Waves* **3** 11–7

[36] Fridman A and Kennedy L A 2011 *Plasma Physics and Engineering* (CRC Press)

[37] den Harder N, van den Bekerom D C M, Al R S, Graswinckel M F, Palomares J M, Peeters F J J, Ponduri S, Minea T, Bongers W A, van de Sanden M C M and van Rooij G J 2016 Homogeneous CO2 conversion by microwave plasma: Wave propagation and diagnostics *Plasma Process. Polym.* 1–24

[38] Van Der Meiden H J, Al R S, Barth C J, Donń A J H, Engeln R, Goedheer W J, De Groot B, Kleyn A W, Koppers W R, Lopes Cardozo N J, Van De Pol M J, Prins P R, Schram D C, Shumack A E, Smeets P H M, Vijvers W A J, Westerhout J, Wright G M and Van Rooij G J 2008 High sensitivity imaging Thomson scattering for low temperature plasma *Rev. Sci. Instrum.* **79** 0–8

[39] Cho Y T and Na S-J 2005 Application of Abel inversion in real-time calculations for circularly and elliptically symmetric radiation sources *Meas. Sci. Technol.* **16** 878–84

[40] Babb J F and Dalgarno A 1995 Radiative association and inverse predissociation of oxygen atoms *Phys. Rev. A* **51** 3021–6

[41] Myers B F and Bartle E R 1968 Shock-tube study of the radiative combination of oxygen atoms by inverse predissociation *J. Chem. Phys.* **48** 3935–44

Supplementary information

Flame Bands: CO + O chemiluminescence as a measure of gas temperature

G. Raposo[1], A.W. van de Steeg[2], E. Mercer[3], C.F.A.M. van Deursen[2], H.J.L. Hendrickx[2], W.A. Bongers[2], G.J. van Rooij[2,4], M.C.M. van de Sanden[2,5] and F.J.J. Peeters[2*]

[1] Instituto Superior Técnico, Lisbon, Portugal
[2] DIFFER, Eindhoven, the Netherlands
[3] University of Antwerp, Antwerp, Belgium
[4] Maastricht University, Maastricht, The Netherlands
[5] Eindhoven University of Technology, Eindhoven, The Netherlands

S.1: Calibration curve of the optical system + half quartz tube

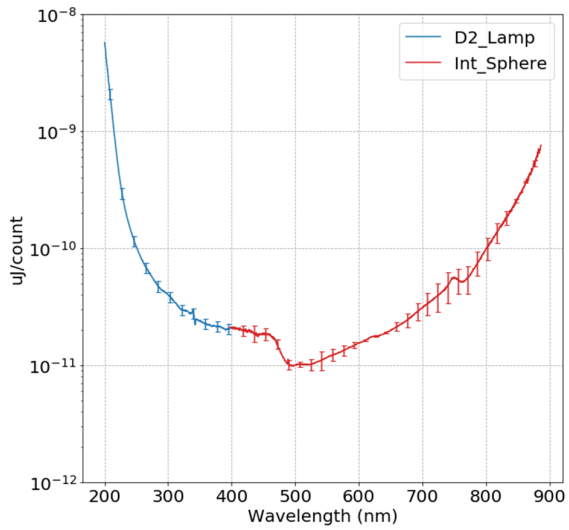

Figure S.1.1: *Calibration curve for the optical system in µJ/count obtained using a halogen lamp with integrating sphere for visible wavelengths (red) and a deuterium lamp in the UV range (blue). A lower value on the y-axis implies a higher sensitivity.*

S.2: Derivations of Eq. (2) and Eq. (8) in the main text

Using the reaction chain R1 – R4, the recombination rate coefficient k_{rec} for the overall reaction R5 can be found from the reaction equations for $CO_2(1\,^1B)$ and $CO_2(1\,^3B)$ and assuming steady-state:

$$\frac{\partial[\mathrm{CO_2}(\,^3\mathrm{B})]}{\partial t} = k_1^+[\mathrm{CO}][\mathrm{O}][\mathrm{M}] - (k_1^-[\mathrm{M}] + k_2^+[\mathrm{M}])[\mathrm{CO_2}(\,^3\mathrm{B})] = 0 \text{ and} \tag{S.1}$$

$$\frac{\partial[\mathrm{CO_2}(\,^1\mathrm{B})]}{\partial t} = k_2^+[\mathrm{CO_2}(\,^3\mathrm{B})][\mathrm{M}] - (k_2^-[\mathrm{M}] + k_3^+[\mathrm{M}] + k_4^+)[\mathrm{CO_2}(\,^1\mathrm{B})] = 0, \tag{S.2}$$

where the simplified notation for the two electronically excited states is used.

Realizing that the change in ground state CO_2 is equal to the rate of reaction R5 and substituting the solutions for $[\mathrm{CO_2}(\,^1\mathrm{B})]$ and $[\mathrm{CO_2}(\,^3\mathrm{B})]$ from (S.1) and (S.2) we get:

$$\frac{\partial[\mathrm{CO_2}]}{\partial t} = k_{rec}[\mathrm{CO}][\mathrm{O}][\mathrm{M}] = (k_3^+[\mathrm{M}] + k_4^+)[\mathrm{CO_2}(\,^1\mathrm{B})]$$

$$= \frac{k_1^+ k_2^+ [\mathrm{M}](k_3^+[\mathrm{M}]+k_4^+)}{(k_1^-[\mathrm{M}]+k_2^+[\mathrm{M}])(k_2^-[\mathrm{M}]+k_3^+[\mathrm{M}]+k_4^+)}[\mathrm{CO}][\mathrm{O}][\mathrm{M}]. \tag{S.3}$$

For the rate coefficient k_γ for the overall reaction leading to photon emission

$$\mathrm{CO}(^1\textstyle\sum_g{}^+) + \mathrm{O}(^3\mathrm{P}) \rightarrow \mathrm{CO_2}(^1\tilde{X}\ \textstyle\sum_g{}^+) + h\nu, \tag{S.R1}$$

it suffices to substitute the solution for $[\mathrm{CO_2}(\,^3\mathrm{B})]$ from (S.2) into (S.1) and obtain a solution for $[\mathrm{CO_2}(\,^1\mathrm{B})]$. Mutiplying this result by the rate coefficient k_4^+ then provides the rate of photon emission:

$$\begin{aligned} I_\gamma &= k_\gamma[\mathrm{CO}][\mathrm{O}] = k_4^+[\mathrm{CO_2}(\,^1\mathrm{B})] \\ &= \frac{k_1^+ k_2^+ [\mathrm{M}] k_4^+ [\mathrm{M}]}{(k_1^-[\mathrm{M}]+k_2^+[\mathrm{M}])(k_2^-[\mathrm{M}]+k_3^+[\mathrm{M}]+k_4^+)}[\mathrm{CO}][\mathrm{O}]. \end{aligned} \tag{S.4}$$

Assuming sponteneous emission via R4 is slower than the (quenching) reaction steps of R2 and R4, the results of Eqs. (S.3) and (S.4) can be further simplified to:

$$k_{rec} = \frac{k_1^+ k_2^+ k_3^+}{(k_1^- + k_2^+)(k_2^- + k_3^+)} \quad \text{and} \tag{S.5}$$

$$k_\gamma = \frac{k_1^+ k_2^+ k_4^+}{(k_1^- + k_2^+)(k_2^- + k_3^+)}, \tag{S.6}$$

so that

$$\frac{k_{rec}}{k_\gamma} = \frac{k_3^+}{k_4^+}. \tag{S.7}$$

For O_2 Schumann-Runge emission, the rate equation for $O_2(^3B)$ via R6 – R8 is:

$$\frac{\partial[\mathrm{O_2}(\,^3\mathrm{B})]}{\partial t} = k_6^+[\mathrm{CO_2}(\,^1\mathrm{B})][\mathrm{O_2}] - (k_7^+[\mathrm{M}] + k_8^+)[\mathrm{O_2}(\,^3\mathrm{B})] = 0, \tag{S.8}$$

which is easily solved to obtain the rate of photon emission from excited O_2:

$$I_\gamma^{O_2} = \frac{k_6^+ k_8^+ [\mathrm{CO_2}(\,^1\mathrm{B})][\mathrm{O_2}]}{k_7^+[\mathrm{M}]+k_8^+} \approx \frac{k_6^+ k_8^+}{k_7^+}\mathcal{X}_{O_2}[\mathrm{CO_2}(\,^1\mathrm{B})] \approx \frac{k_6^+ k_8^+}{k_4^+ k_7^+}\mathcal{X}_{O_2} \cdot k_\gamma[\mathrm{CO}][\mathrm{O}]. \tag{S.9}$$

As (S.9) shows, the rate of UV photon emission will be proportional to photon emission from CO + O recombination, scaled by the O_2 fraction in the gas.

Alternatively, if $O_2(^3B)$ results from quenching of $[\mathrm{CO_2}(\,^3\mathrm{B})]$ by O_2 via

$$\mathrm{CO_2}(^3\mathrm{B}) + \mathrm{O_2} \rightarrow \mathrm{CO_2} + \mathrm{O_2}(^3\mathrm{B}), \tag{S.R2}$$

we get:

$$\frac{\partial[\mathrm{O_2}(\,^3\mathrm{B})]}{\partial t} = k_{A.R3}^+[\mathrm{CO_2}(\,^3\mathrm{B})][\mathrm{O_2}] - (k_7^+[\mathrm{M}] + k_8^+)[\mathrm{O_2}(\,^3\mathrm{B})] = 0, \tag{S.10}$$

which can be solved by substituting the result of (S.1) to obtain an alternative rate of photon emission $I'^{O_2}_{\gamma}$:

$$I'^{O_2}_{\gamma} = \frac{k^{+}_{S.R2}k^{+}_{8}[\mathrm{CO_2}(\,^3\mathrm{B})][\mathrm{O_2}]}{k^{+}_{7}[\mathrm{M}]+k^{+}_{8}} = \frac{k^{+}_{1}k^{+}_{S.R2}k^{+}_{8}[\mathrm{O_2}]}{(k^{-}_{1}+k^{+}_{2})(k^{+}_{7}[\mathrm{M}]+k^{+}_{8})}[\mathrm{CO}][\mathrm{O}] \approx \frac{k^{+}_{1}k^{+}_{S.R2}k^{+}_{8}}{(k^{-}_{1}+k^{+}_{2})k^{+}_{7}}\mathcal{X}_{O_2}[\mathrm{CO}][\mathrm{O}], \qquad \text{(S.11)}$$

which has the same general features as (S.9).

S.3 Values of Arrhenius model

Table S.1: *Tabulated values from Arrhenius fits displayed in Figure 6 of the main text.*

$\boldsymbol{\lambda}$ [nm]	$\boldsymbol{k_0^{\lambda}}$ [10^{-27} γ.m^{3}s^{-1}nm^{-1}]	$\boldsymbol{\Delta k_0^{\lambda}}$ [10^{-27} γ.m^{3}s^{-1}nm^{-1}]	$\boldsymbol{E_a^{\lambda}}$ [K]	$\boldsymbol{\Delta E_a^{\lambda}}$ [K]
246.5	16.415	3.92132	5766	120.9
255.9	16.0996	3.41351	5399	107.8
265.4	15.2869	2.71347	5007	91.11
274.8	13.988	2.07875	4591	76.89
284.3	12.4721	1.51714	4188	63.48
293.6	10.8797	1.05643	3781	50.99
303	9.44795	0.68466	3411	38.48
312.3	8.12461	0.43003	3065	28.31
321.7	7.01463	0.25935	2752	19.88
331	6.15028	0.15927	2487	14.05
340.2	5.4499	0.08542	2253	8.493
349.5	4.83653	0.09163	2051	10.38
358.7	4.35227	0.09219	1884	11.64
367.8	3.92159	0.09918	1738	13.99
377	3.53459	0.10552	1613	16.63
386.1	3.20335	0.11108	1510	19.35
395.2	2.92706	0.12281	1430	23.37
404.3	2.63952	0.11351	1345	24.25
413.4	2.39025	0.11172	1277	26.55
422.4	2.1758	0.10662	1226	27.75
431.4	2.00511	0.10141	1185	28.84
440.4	1.84448	0.09381	1156	28.87
449.3	1.69486	0.08878	1124	29.88
458.2	1.56894	0.08297	1102	30.18
467.1	1.45586	0.07703	1086	30.28
476	1.3652	0.06988	1085	29.37
484.8	1.28711	0.06198	1088	27.41
493.6	1.19877	0.05717	1088	26.98
502.4	1.10672	0.05433	1071	27.9
511.2	1.03169	0.05257	1072	28.86
519.9	0.96387	0.04508	1081	26.56
528.6	0.90746	0.04118	1094	25.79

537.2	0.85035	0.03872	1099	25.95
545.9	0.7827	0.03768	1088	27.55
554.5	0.72513	0.03663	1085	28.94
563	0.68523	0.03738	1103	31.18
571.6	0.6414	0.03229	1108	28.92
580.1	0.59852	0.03086	1113	29.68
588.6	0.5561	0.02914	1107	30.29
597	0.52241	0.02909	1114	32.21
605.5	0.49115	0.02493	1119	29.52
613.9	0.46575	0.02526	1139	31.51
622.2	0.43867	0.02098	1141	27.83
630.6	0.4147	0.02127	1153	29.96
638.9	0.39047	0.01891	1156	28.37
647.1	0.36891	0.01904	1162	30.28
655.4	0.35011	0.01722	1170	28.92
663.6	0.33244	0.01506	1179	26.72
671.8	0.31695	0.01418	1198	26.47
679.9	0.30222	0.01292	1216	25.29
688	0.28921	0.01129	1240	23.11
696.1	0.27912	0.01115	1272	23.66

S.4 Example Arrhenius model fits

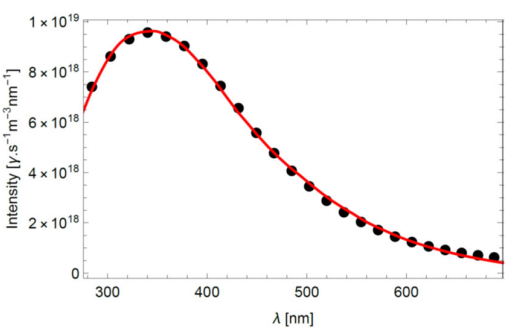

Figure S.2: Spectrum fit for 300 mbar, 6 slm at r = -4 mm and z = 53 mm. Fitted temperature is (1869.65 ± 45.81) K.

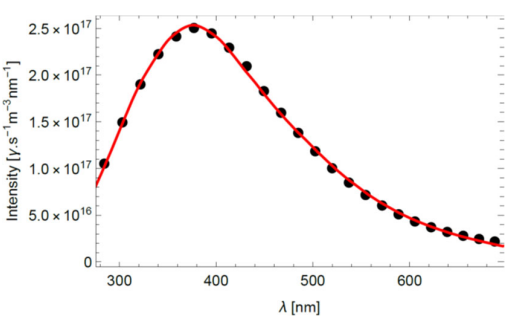

Figure S.2: Spectrum fit for 100 mbar, 12 slm at r = -2 mm and z = 53 mm. Fitted temperature is (1260.02 ± 22.69) K.